

Article

Force Transfer Mechanism and Component-Based Model of Cast-Steel-Stiffened Circular-Tube-Column Frames for Progressive Collapse Analysis

Xinxia Li ^{1,*}, Lan Tao ¹ and Mingjie Liu ²

¹ School of Civil and Transportation Engineering, Beijing University of Civil Engineering and Architecture, Beijing 100044, China; taolan@163.com

² Department of Civil Engineering, Tianjin University, Tianjin 300072, China; liumingjie@tju.edu.cn

* Correspondence: lixixiaky@163.com

Abstract: In this paper, the system response, stress redistribution, failure mode, and catenary effect of steel frames with circular tube columns and cast steel stiffener (CSS) joints under a sudden column removal scenario were revealed. Based on this force transfer mechanism analysis, a practical and computationally efficient component-based model considering catenary effects and CSS joint details with a series of springs was established and validated by a detailed solid-element method. By using this component-based model, the proper dynamic response increase factor of the CSS joint frames was investigated. The results show that the great overall stiffness and strength of the CSS limit the deformation of the column front shell. Therefore, the CSS joint frames have superior performance for progressive collapse prevention than the frames using welded joints without stiffeners. In addition, the component-based model is validated to be effective and the dynamic response increase factor of the frames with circular tube columns and CSS joints is smaller than 2.0.

Keywords: component-based model; circular-tube-column frame; dynamic increase factor; column removal scenario; cast steel stiffener



Citation: Li, X.; Tao, L.; Liu, M. Force Transfer Mechanism and Component-Based Model of Cast-Steel-Stiffened Circular-Tube-Column Frames for Progressive Collapse Analysis. *Buildings* **2022**, *12*, 1049. <https://doi.org/10.3390/buildings12071049>

Academic Editor: André Furtado

Received: 19 June 2022

Accepted: 13 July 2022

Published: 20 July 2022

Publisher's Note: MDPI stays neutral with regard to jurisdictional claims in published maps and institutional affiliations.



Copyright: © 2022 by the authors. Licensee MDPI, Basel, Switzerland. This article is an open access article distributed under the terms and conditions of the Creative Commons Attribution (CC BY) license (<https://creativecommons.org/licenses/by/4.0/>).

1. Introduction

Progressive collapse is a complex dynamic process in which initial localized damage extends from one element to another, eventually leading to a disproportionately large portion of collapse of a structure, or even complete collapse [1]. The progressive collapse incident of the Ronan Point apartment that occurred in 1968 [2] in the UK was a wake-up call for the world. After that, researchers conducted a series of studies [3–31] to develop structural design for the prevention of such failures in the future.

Beam-column joints, which serve as force transmission hubs, are key components for progressive collapse prevention. For circular-tube-column frames, the construction of beam-column joints is quite different from that of H-shaped steel columns. In recent years, researchers have conducted a great deal of work on the H-shaped beam to circular-tube-column joints [32–38]. A cast steel stiffener (CSS) joint which is suitable for circular tube columns was investigated by Liu et al. [38] using numerical analysis and experimental study under cyclic loading. This CSS joint can reduce the welding quantity at the intersection of the components and rationalize the stress distribution by a reasonable cross-sectional shape, and was verified to have high rigidity and good seismic performance. However, there is still a lack of research on the performance of circular-tube-column frames with such CSS joints to resist progressive collapse.

On the other hand, the model for simulating the CSS joint frame under a column removal scenario can be a detailed solid-element model considering joint details and progressive collapse issues. However, the detailed solid-element model is computationally expensive. A beam model with ideal rigid joints is a reasonably efficient model, but the

detailed characteristics of the CSS joint frame are hard to be represented adequately with such a model. Therefore, a computationally efficient model considering catenary effects and CSS joint details was needed for practical analysis.

Several researchers have applied component-based models in some progressive collapse analyses for different structures. The component-based model is a kind of model that consists of a series of discrete spring elements, rigid elements, and beam elements. The component-based model has the features of saving computation time, analyzing the overall response of the structure, as well as highlighting the primary details of a structure [39]. For example, Lee et al. [40] proposed a parallel axial–flexural point plastic hinge model to consider the catenary effect of a two-span steel frame with H-shaped beams and columns under a sudden column removal scenario in an efficient way. Yu and Tan [41] proposed a component-based joint model with a series of springs to simulate the structural responses of specimens with severe geometric and material nonlinearity for reinforced concrete structures in progressive collapse analysis. Bao et al. [42] proposed a component-based model of a beam–column joint to represent the critical and essential actions in beams and the transfer of the actions through joints to vertical components. This simplified simulation model was evaluated by high-fidelity finite element analysis. Fu et al. [43] proposed a component-based model of steel joints to study the performance of two-dimensional bolted-angle steel frames subject to a sudden column failure by the alternative load path method. Zhao et al. [44] established a simplified joint model to investigate the progressive collapse behavior of post-tensioned energy-dissipating joints in steel frames. Liu et al. [45] developed a component-based model to investigate the dynamic performance of bolted-angle joints in progressive collapse. Stylianidis and Nethercot [46] also described the behavior of steel joints in progressive collapse by developing a mechanical approach. These studies verified that different kinds of beam–column joints can be effectively simulated by appropriate component-based models. However, the research on a suitable component-based model for steel frames with circular tube columns and cast steel stiffeners is still limited.

In this paper, an in-depth analysis was conducted to investigate the initial stiffness and stiffness degradation rule of CSS joints, as well as the bending moment–axial force interactive relationship at beam ends, for frames with circular tube columns and CSS joints under a column removal scenario. The CSS joint was creatively assembled and represented by a series of springs and beam elements. A computationally efficient component-based model for the CSS steel frame with circular tube columns was then proposed and used to investigate the dynamic response increase factor for the design in practice to resist progressive collapse.

2. Prototype Frame for Progressive Collapse Analysis

In accordance with Chinese design codes [47,48], a prototype two-story steel moment frame was designed to investigate the performance of CSS frames to resist progressive collapse. The plan view and elevation view of this two-story steel frame are shown in Figure 1. In the frame, the dimensions of H-shaped beams are $194 \times 150 \times 6 \times 9$ mm, in which the numbers are the depth, flange width, web thickness, and flange thickness of the H-shaped beam, respectively. The circular steel tube column has an outer diameter of 203 mm and a wall thickness of 12 mm. The frame spans in the x and y axes are 4000 mm and 3800 mm, respectively. The height of each floor is 3000 mm.

The prototype two-story frame was designed to have welded joints and CSS joints. G20Mn5 steel was used for the cast steel stiffeners, and HRB235 steel was used for the columns and beams.

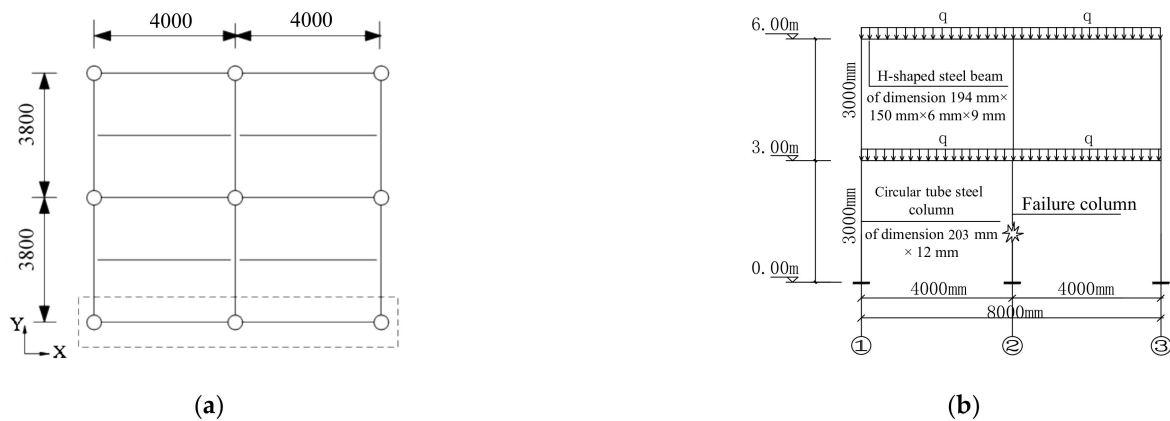


Figure 1. Two-story circular-tube-column frame (unit: mm). (a) Plan view; (b) Elevation view.

3. Detailed Solid-Element Model and the Force Transfer Mechanism of CSS Joint Frame in Progressive Collapse

3.1. Detailed Solid-Element Model for Collapse

Detailed solid-element model A_c and model B_c were established by ABAQUS software to simulate the boxed area of the prototype two-story frame in Figure 1a, as shown in Figure 2. Model A_c is a circular-tube-column frame with welded joints, and model B_c is a circular-tube-column frame with CSS joints. These plane frame models are commonly used models for in-depth analysis of structural performance against progressive collapse [1,49].

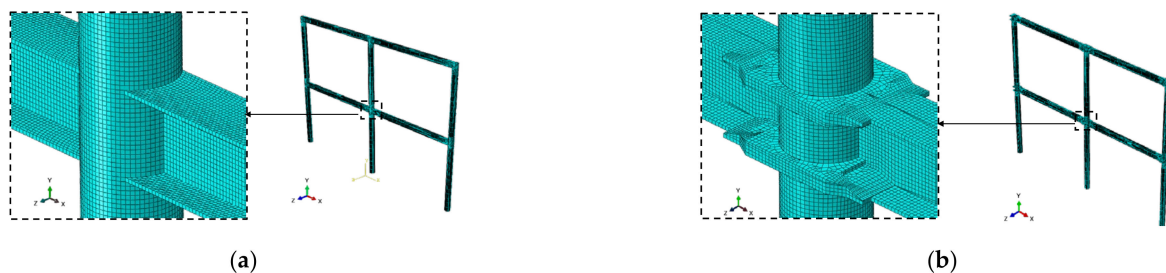


Figure 2. Detailed models of circular-tube-column frames with different joints: (a) Model A_c ; (b) Model B_c .

The dimensions of the CSS for circular tube columns are shown in Figure 3. The CSS consists of a ring plate provided with prefabricated welding grooves, flanges, and stiffening ribs. The reinforcing ribs are rounded to reduce the stress concentration in the CSS.



Figure 3. CSS for circular-tube-column frame (unit: mm): (a) Three-dimensional diagram; (b) Three orthographic views.

In model B_c (shown in Figure 2b), the ring plate and the circular tube column are connected by non-penetration butt welds applied along the pre-formed welding grooves. Beam webs are connected to column webs by two-side fillet welds. Moreover, beam flanges are connected to CSS flanges by butt welds. The flat surface of the upper CSS has the same height as the upper surface of the beam flange.

C3D8R elements were used in all the components with an approximate mesh size of 0.01 m (shown in Figure 2); bilinear material models were used for all components and the material parameters of the bilinear models of all components were obtained through material performance tests conducted in reference [38]; all degrees of freedom at column bottoms were constrained before the sudden column removal process. For dynamic alternative load path method (APM) analysis, 1.2 DL + 0.5 LL transformed into mass was applied to the frame according to DOD 2010 [1], where DL and LL are dead load and live load, respectively. The gravity loads were slowly ramped up over a 10 s period. After the 10 s period, the loads have been held constant for an additional 3 s to damp out the dynamic effects. In the next step, the sudden failure of the column was simulated by freeing the vertical support restraint at the interior column bottom within 0.001 s. At last, the simulation continued for 2 more seconds. A 5% mass proportional damping was adopted in this simulation.

The accuracy of this detailed solid-element modeling method has been validated by a test of a CSS joint frame under a sudden interior column removal scenario in reference [50] conducted by the author of this paper. By using this method, a comparison of different detailed solid-element models (i.e., three-dimensional (3D) frame with slabs, 3D frame without slabs, and plane frame) to simulate the test frame in reference [50] is conducted further in this paper, the displacement–time curves of different detailed solid-element models are demonstrated in Figure 4.

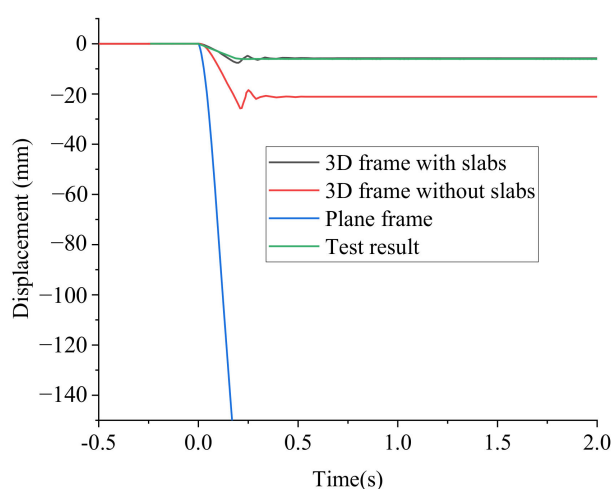


Figure 4. Displacement–time curves of different detailed solid-element models simulating the test.

Figure 4 shows that the result of the 3D frame with slabs is in good agreement with the test result. The other two models will overestimate the displacement of the interior column in progressive collapse. This displacement result indicates that the out-of-plane pulling actions from orthogonal beams and the rigidity of slabs on the progressive collapse performance of steel moment frames are significant, which helps the structure to resist progressive collapse. Therefore, the plane frame model used in this paper is relatively conservative in comparison to 3D models.

3.2. System Response under Different Load Cases

A series of increasing loads were applied on plane frame models of model A_c and model B_c to simulate the system responses to sudden column loss under different scenarios. To demonstrate and compare the different performances of model A_c and model B_c under

the same load, four typical load cases (shown in Table 1) were selected. According to the load code for the design of building structures in China [48], load case (i) represents the load of a light non-accessible slab/roof; load case (ii) represents the load of a normal accessible slab/roof; load case (iii) represents the load of a heavy accessible slab/roof with large live load, such as the load of crowded cabinets in the libraries; and load case (iv) represents the load of a heavy accessible slab/roof with extremely large live load, such as fire vehicle load.

Table 1. Load cases.

Load	Dead Load ($\text{kN}\cdot\text{m}^{-2}$)	Live Load ($\text{kN}\cdot\text{m}^{-2}$)
i	1.0	0.5
ii	3.2	2.0
iii	5.1	12.0
iv	5.1	20.0

Under the loads in Table 1, displacement–time history curves of the interior column bottoms of model A_c and model B_c are shown in Figure 5, and the maximum and final values of each displacement curve are listed in Table 2. Table 3 lists the time when the plastic strain occurred in model A_c and model B_c under different load levels.

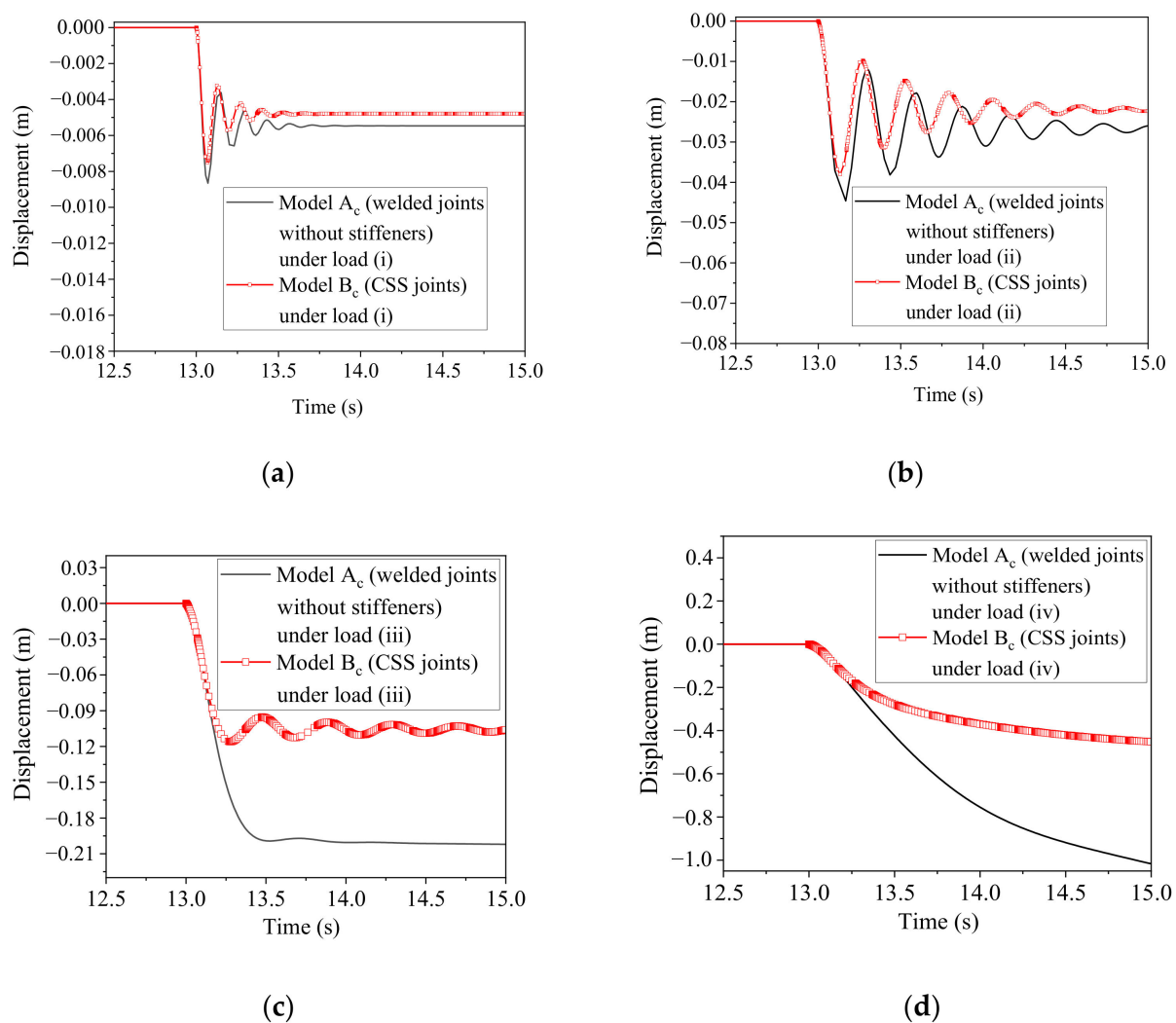


Figure 5. Displacement–time history curves of the interior column bottoms in models A_c and B_c : (a) Load (i); (b) Load (ii); (c) Load (iii); (d) Load (iv).

Table 2. Displacements of the interior column bottoms in models A_c and B_c.

Load	Maximum Displacement (mm)		Final Displacement (mm)	
	Model A _c	Model B _c	Model A _c	Model B _c
i	−8.65	−7.49	−5.47	−4.80
ii	−44.61	−38.02	−25.96	−22.34
iii	−202.04	−115.99	−202.04	−105.97
iv	−1016.92	−451.97	−1016.92	−451.97

Table 3. The time when the plastic strain occurred in model A_c and model B_c.

Load	The Time When Plastic Strain Occurred (s)	
	Model A _c	Model B _c
i	-	-
ii	13.059	13.071
iii	13.052	13.054
iv	13.052	13.054

Figure 5, Tables 2 and 3 show that in the column removal analysis, model A_c and model B_c are elastic under load (i). Under load (i), compared with welded joints, beam-column joints with CSS reduce the maximum and final vertical displacement values of the bottom of the interior column by 13.41% and 12.24%, respectively.

Under load (ii), compared with welded joints, beam-column joints with CSS delay the occurrence of the plastic deformation of structures and reduce the maximum and final vertical displacement values of the bottom of the interior column by 14.77% and 13.94%, respectively.

Under load (iii), these two models undergo plastic deformation at approximately the same time. Compared with welded joints, beam-column joints with CSS reduce the final vertical displacement value of the bottom of the interior column by 47.55%.

Under load (iv), these two models undergo plastic deformation at approximately the same time. The vertical displacements of the interior column bottoms of model A_c and model B_c initially increased rapidly and then increased slowly because of the catenary effect. Compared with welded joints, beam-column joints with CSS reduce the final vertical displacement value of the bottom of the interior column by 55.56%.

In summary, the performance of steel frames with beam-column joints using CSS is better than that of steel frames with welded joints for progressive collapse prevention, whether the frame is elastic, plastic, or collapsed after the sudden failure of the interior column.

3.3. Force Transfer Mechanism

3.3.1. Stress Redistribution

In order to further illustrate the differences in equivalent plastic strain redistribution and stress redistribution between steel frames with welded joints and CSS joints, models A_c and B_c under load (iii) were demonstrated as examples.

The corresponding equivalent plastic strain redistribution and stress redistribution of model A_c at 15 s are shown in Figures 6 and 7, respectively. Figures 6 and 7 show that the stress concentration region is located at the corner where the flange of the beam end and the column are connected. Due to the tensile force of the beam flange, the column bears a large axial force, which results in an obvious buckling. The maximum equivalent plastic strain of model A_c is 0.0636. The deformation of the joints and beam ends of the frame presents a “V”-shaped curve after the sudden failure of the interior column.

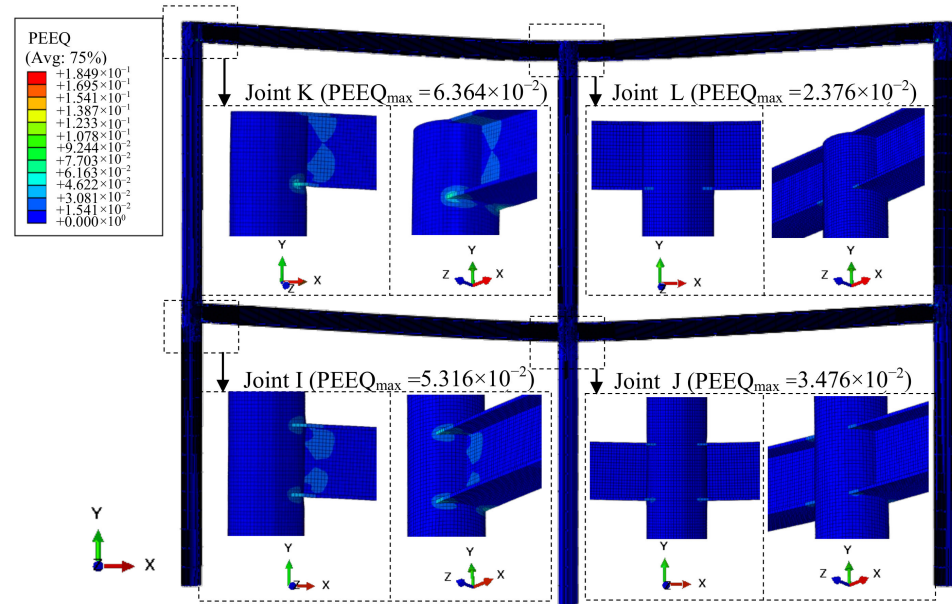


Figure 6. Equivalent plastic strain cloud diagram of model A_c at 15 s under load (iii).

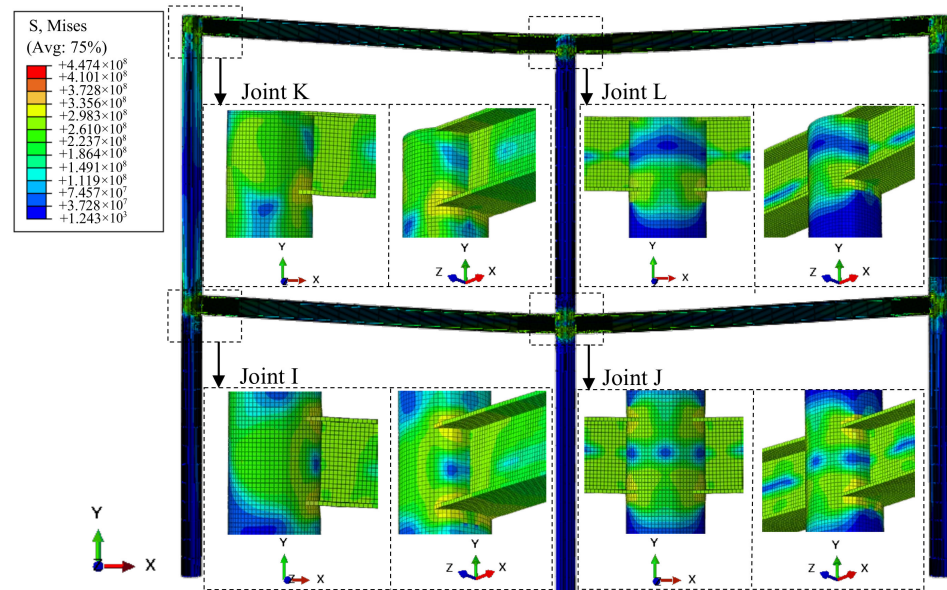


Figure 7. Mises stress cloud diagram of model A_c at 15 s under load (iii).

The corresponding equivalent plastic strain redistribution and stress redistribution of model B_c when the maximum displacement occurred are shown in Figures 8 and 9, respectively. The result shows that the stress concentration region occurs mainly at the CSS. This is due to the fact that the CSS has relatively high strength and rigidity and bears a large portion of the tension load transmitted from the beam end, so the tension load borne by the column front shell is reduced, avoiding large strains in the column front shell. The maximum equivalent plastic strain of model B_c is 0.0232, and the obvious deformation is mainly concentrated at the beam end rather than the column. Due to the large rigidity of the beam-column joint with CSS, which restricts the joint deformation, the deformation of the frame presents a relatively smooth “U”-shaped curve after the sudden failure of the interior column.

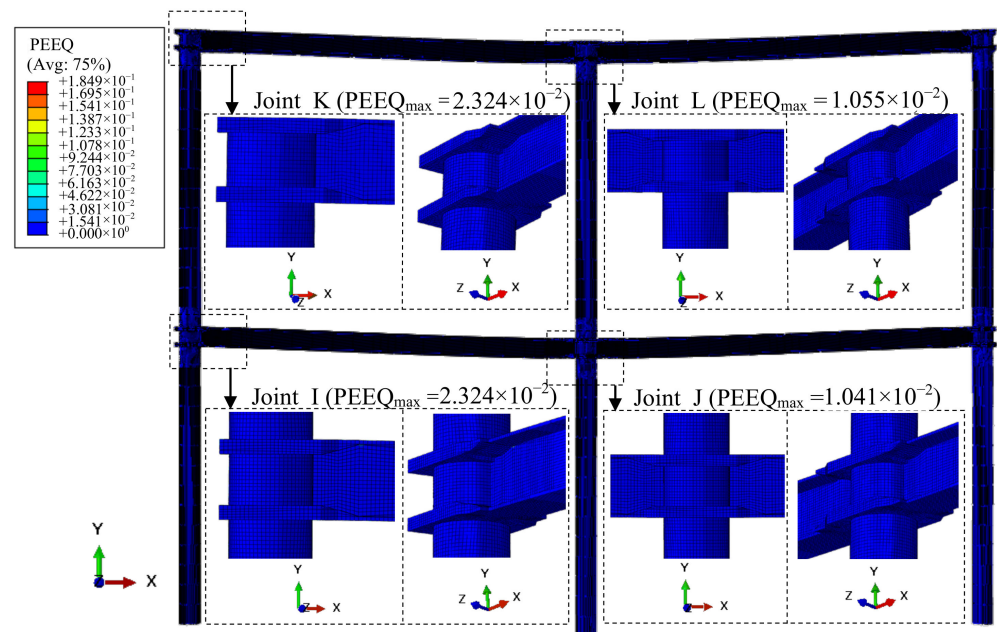


Figure 8. Equivalent plastic strain of model B_c when the vertical displacement of the interior column reached its maximum value under load (iii).

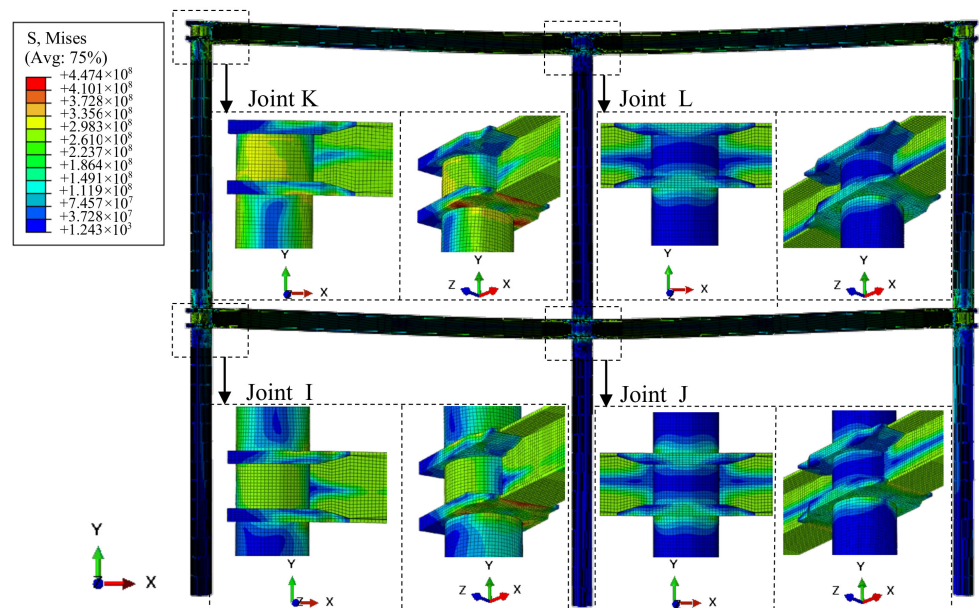


Figure 9. Mises stress of model B_c when the vertical displacement of the interior column reached its maximum value under load (iii).

3.3.2. Failure Mode

To illustrate the different failure modes of model A_c and model B_c in progressive collapse, the time history curves of the maximum equivalent plastic strains at the buckled regions and the interior column displacements of the two frames under load (iv) are presented in Figure 10. In Figure 10a, significant local buckling develops with the increase of the interior column displacement; in Figure 10b, only slight local buckling develops after the sudden column removal. The different failure modes of these two models result in a larger increase in displacement for model A_c than for model B_c.

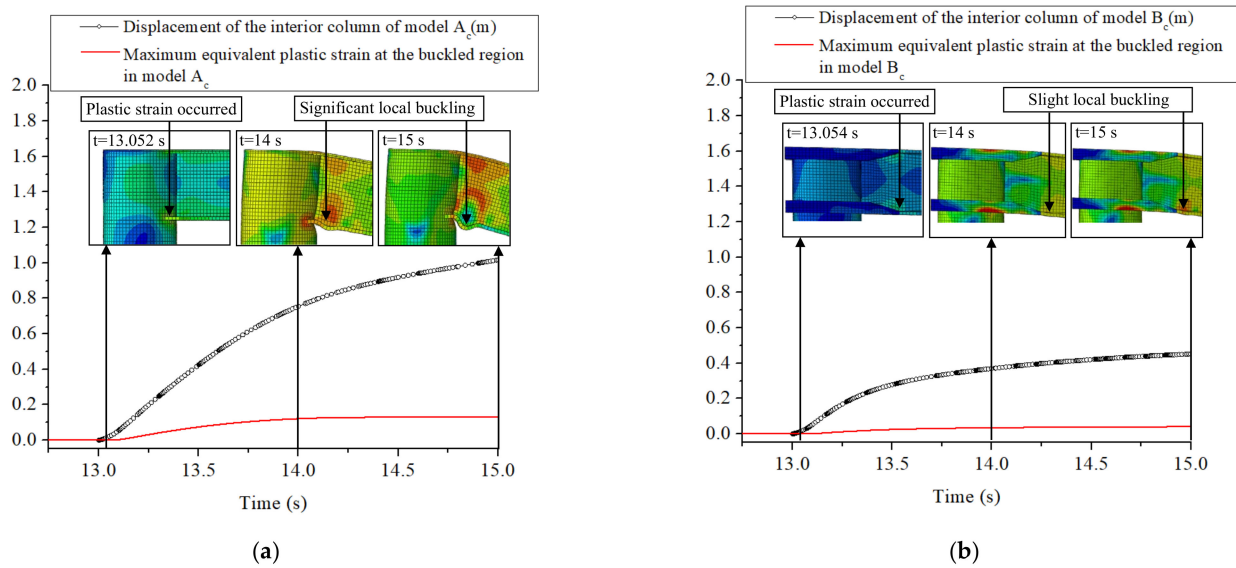


Figure 10. Time history curves of the displacements of the interior columns and the maximum equivalent plastic strains at the buckled regions under load (iv): (a) Model A_c; (b) Model B_c.

3.3.3. Axial Tension–Bending Moment Interaction at Beam Ends

Figure 10b shows that the final damage of model B_c is caused by the plastic hinge occurring at the beam ends connected to the outer side of the CSS flange. In order to study the axial force–bending moment interaction at beam ends, model S (shown in Figure 11a), a subassembly two-span frame, was extracted from model B_c. A vertical loading method was applied to the top section of the interior column with a load rate of 2 mm/min until the final vertical downward displacement reached 2 m. The rotations and displacements of the bottom and top sections of the corner columns were restricted. The column was set as a rigid body to prevent joint damage from occurring earlier than the damage to the beam. Figure 11b shows the distribution of the equivalent plastic strain for model S.

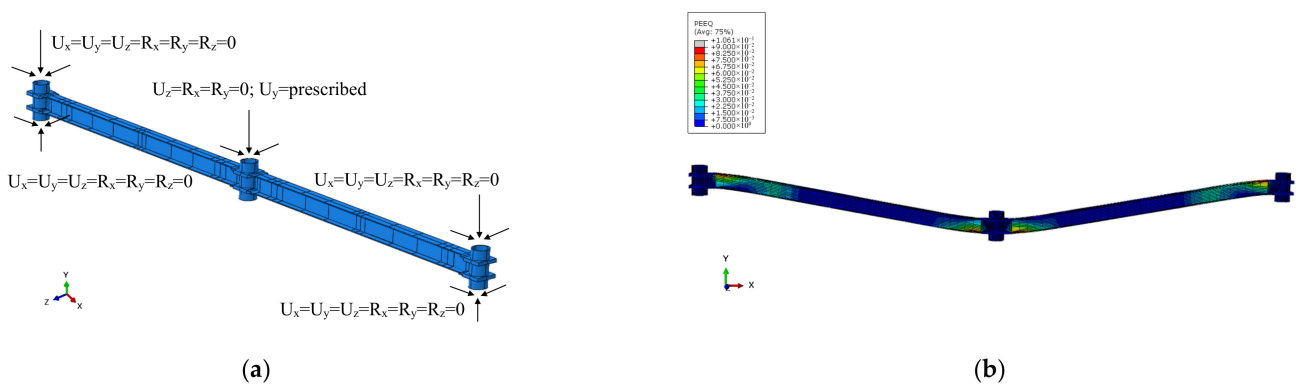


Figure 11. Subassembly two-span frame extracted from model B_c (model S): (a) Boundary conditions; (b) Equivalent plastic strain distribution.

In Figure 11b, plastic hinges develop at both ends of the beams. The axial tension (T) and bending moment (M) at beam ends are normalized by the plastic bending moment (M_p) and the tensile yield strength (T_y) of the beam, respectively. The (T/T_y) and (M/M_p) on the ordinate axis are shown in Figure 12. In Figure 12, steel beams are gradually transformed from bending members into tension–bending members with the increase of the column displacement. Finally, the subassembly frame relies on the internal axial tension of the beams to resist progressive collapse. This is a typical catenary effect process [51].

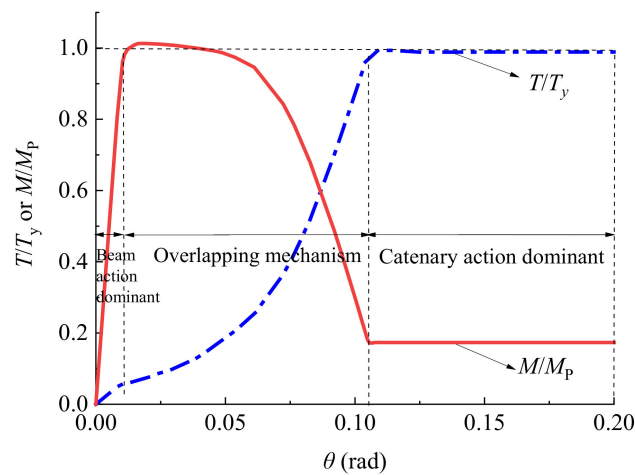


Figure 12. Axial tension–bending moment interaction at beam ends of model S.

To sum up, the greater overall stiffness and strength of the CSS limit the deformation of the column front shell, which results in a very different stress redistribution and deformation pattern in CSS joints compared with welded joints. In the CSS joint frame, plastic hinges at beam ends appear at locations farther away from columns, thus changing the deformation pattern of the whole frame after the sudden failure of the interior column. Moreover, the bending moment–axial tension interaction relationship of the plastic hinge region indicates that the frame still exhibits the catenary effect even if the plastic hinge region is moved outward.

4. Component-Based Model for Frames with Circular Tube Columns and CSS Joints

In practice, detailed solid-element models are time-consuming and complicated, even for the detailed solid-element model of a plane frame. Therefore, establishing a practical and efficient component-based model that fully considers the force transfer mechanism and the special construction of the CSS joint for progressive collapse analysis is necessary.

In the circular-tube-column joint, the load (M) applied to the joint is mainly borne by the CSS due to its large stiffness, and only negligible load is borne by the web. Therefore, the load (M) can be simplified as h_b multiplied by F , where h_b is the distance between the centers of the lower and upper flanges of the beam and F is the compression/tension force on the CSS (shown in Figure 13).

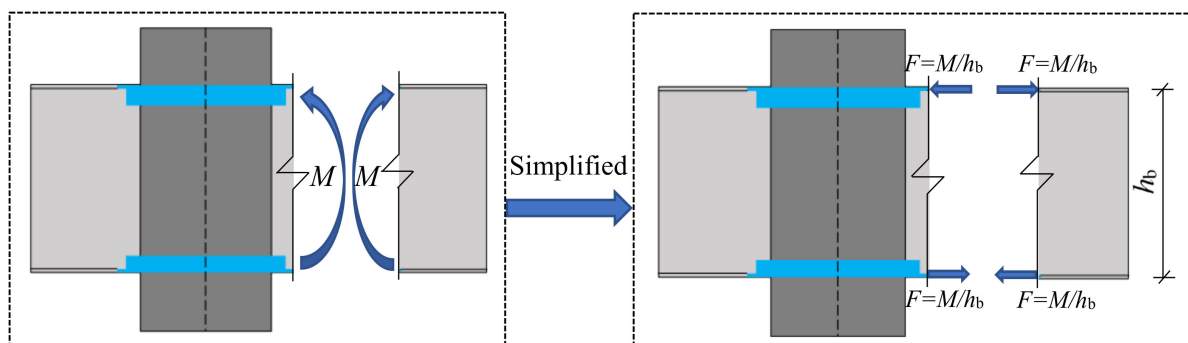


Figure 13. Schematic diagram of the simplified process of the load.

Based on this simplified principle, the component-based model can be constructed. First, four rigid rods should be hinged together to simulate the panel zone of the column to meet the corresponding deformation requirements; a diagonal spring should be used to connect two diagonal points of the panel zone to simulate its deformation; and a rotation

spring should exist to represent the deformation of the CSS ring and column front shell. Second, a plastic deformation region with rotational springs and tension–compression springs should exist to represent the shearing and bending resistance of the beam end. Third, a rigid member should be arranged between the panel zone and the plastic deformation region of the beam to represent the relatively high rigidity of the CSS fringe. In addition, other regions of the beams and columns in the frames can be simulated by beam elements. Based on this analysis, the frame studied in Section 3 can be simplified to a component-based model shown in Figure 14.

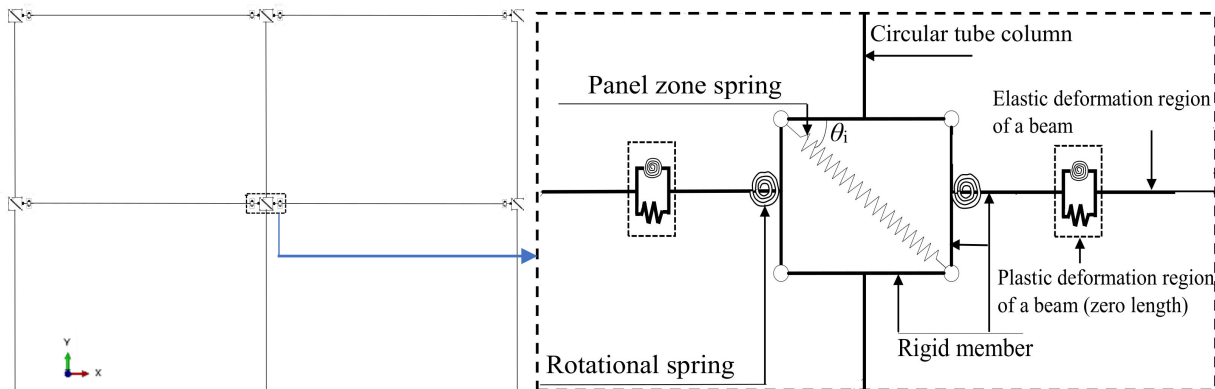


Figure 14. Component-based model of the frame with circular tube columns and CSS joints.

4.1. Plastic Deformation Region Properties at Beam End

In order to consider the catenary effect, the plastic deformation region of a beam in the component-based model is combined with a plastic hinge model with a tension–bending spring [40], which was proposed by Lee et al. The model assumes that the column and the joint section are rigid, so all inelastic deformations occur at beam ends. The applicability of this model to simulate the catenary effect of any H-shaped beam without considering the details of the joints was validated in reference [40].

4.2. Force–Displacement Interaction Relationship of Joint Springs

4.2.1. Initial Stiffness of Joint Springs

a. Rotational spring

The relative deformation of the lower and upper CSS on one side of the joint will cause the section to rotate, which can be simulated by a rotational spring. The initial rotational stiffness of the spring simulating the deformation of CSS can be deduced as detailed below.

The displacement of the CSS (Δl_1^c) is shown schematically in Figure 15. The experimental and numerical analyses in reference [38] revealed that for the H-shaped beam to circular-tube-column joints with CSS, the external tension/compression force on the CSS is borne by the CSS and the column front shell, and the deformations of them are coordinated, so the load can be distributed according to the tensile stiffness ratio of the ring plate of CSS to the column front shell. According to the analysis and deduction from the literature [38], the relationship between the force F_s distributed to the CSS and the total force F is expressed as

$$F_s = \frac{F}{1 + \frac{L_s}{2E_s A_s} \cdot \frac{D}{X_c L L_1}} \quad (1)$$

$$X_c = \frac{\sum_{m=1,3,5,\dots}^{\infty} \sum_{n=1,3,5,\dots}^{\infty} \frac{4[(\frac{m\pi}{L})^2 + (\frac{n\pi}{L_1})^2]^2 \sin^2 \frac{m\pi}{2} \sin^2 \frac{n\pi}{2}}{(L L_1)^2 [(\frac{m\pi}{L})^2 + (\frac{n\pi}{L_1})^2]^4 + \frac{E_c t}{R^2 D} (m\pi)^4 (\frac{L_1}{L})^2}}{\quad} \quad (2)$$

where E_s is the elastic modulus of the CSS; and L_s/A_s is the ratio of the length to the cross-sectional area of the ring plate of the CSS in the force direction. Due to the complex

shape of the CSS for the circular-tube-column joint, it needs to be calculated by integration; D is the unit bending stiffness of the cylindrical front shell of the circular tube column; X_c is a dimensionless parameter; L is the bus length of the cylindrical front shell; L_1 is the arc length of the cylindrical front shell; R is the radius of the middle surface of the cylindrical front shell; t is the thickness of the cylindrical front shell; and E_c is the elastic modulus of the column.

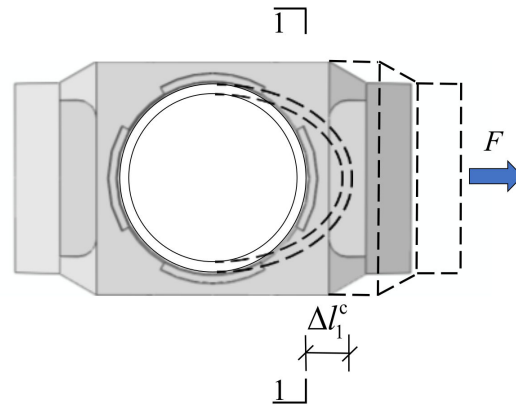


Figure 15. Schematic diagram of Δl_1^c .

Based on Equation (2), the displacement of the CSS (Δl_1^c) is given as

$$\Delta l_1^c = \frac{F_s}{E_s A_s} L_s = \frac{F}{1 + \frac{L_s}{2E_s A_s} \cdot \frac{D}{X_c L L_1}} \cdot \frac{L_s}{E_s A_s} \quad (3)$$

Based on Equation (3), the calculation equation for the initial rotational stiffness of the joint rotation spring (k_s^c) is given as:

$$k_s^c = \frac{M}{\theta_{CSS}} = \frac{F h_b}{\frac{2\Delta l_1^c}{h_b}} = \frac{h_b^2 E_s A_s}{2L_s} + \frac{h_b^2 D}{4X_c L L_1} \quad (4)$$

where M is the bending moment on one side of the joint; θ_{CSS} is the rotation angle on one side of the joint; and h_b is the distance between the centers of the lower and upper flanges of the H-shaped beam.

b. Panel zone spring

In order to obtain the deformation of the panel zone spring, the horizontal displacement of the column at the position of the CSS (Δl_2) should be analyzed first. Δl_2 is shown in Figure 16. The displacement of the column at the position of CSS is composed of two parts, namely, the deformations caused by the bending moment and shearing force of the steel tube column. Therefore, the deformation Δl_2 is given as

$$\Delta l_2 = \frac{F h_b^2 (l_1^3 + (l_2 - h_b)^3)}{6E_c I_c (l_1 + l_2)(l_1 + l_2 - h_b)} + \frac{F k_c h_b (l_1 + l_2 - h_b)}{2G_c A_c (l_1 + l_2)} \quad (5)$$

where A_c is the cross-sectional area of the column; k_c is the shear correction coefficient; G_c is the shear modulus; I_c is the inertia moment of the column section; l_1 is the distance from the midpoint of the upper layer to the center of the upper beam flange; and l_2 is the distance from the midpoint of the layer in which the beam is included (if this layer is the ground layer, then to one-third of the height of this layer) to the center of the upper beam flange.

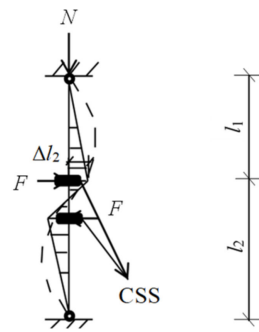


Figure 16. Schematic diagram of Δl_2^c .

The deformation schematic diagram of the panel zone spring is shown in Figure 17, where θ_i is the interior angle of the horizontal rigid member to the diagonal panel zone spring, which is given as

$$\frac{1}{\cos^2 \theta_i} = \frac{(B-t)^2 + h_b^2}{(B-t)^2} \quad (6)$$

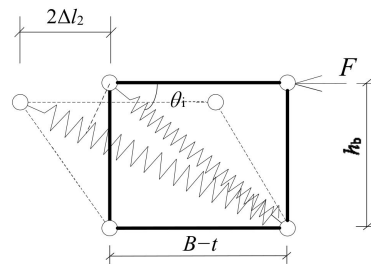


Figure 17. Deformation schematic diagram of the panel zone spring.

Then, the calculation equation of the initial rotational stiffness of the spring simulating the deformation of the panel zone (k_{pz}^s) is given as

$$\begin{aligned} k_{pz}^s &= \frac{F}{2\Delta l_2} \times \frac{1}{\cos^2 \theta_i} \\ &= \frac{1}{\frac{h_b^2(l_1^3 + (l_2 - h_b)^3)}{3E_c I_c (l_1 + l_2)(l_1 + l_2 - h_b)} + \frac{k_c h_b (l_1 + l_2 - h_b)}{G_c A_c (l_1 + l_2)}} \times \frac{1}{\cos^2 \theta_i} \end{aligned} \quad (7)$$

In order to validate the applicability of the joint springs in the component-based model, the joint test results of the specimens with column thicknesses of 8 mm, 10 mm, and 12 mm in the literature [38] are taken as examples. The specimens are cross joints with circular tube columns, H-shaped beams, and CSS joints. The detailed solid-element model and the component-based model established in this paper for simulating these specimens are shown in Figure 18a,b, respectively. The initial rotational stiffness of test specimens, the detailed solid-element models, and the component-based models are listed in Table 4.

Table 4. Initial rotational stiffness of the test specimens, the detailed solid-element models, and the component-based models.

Specimen	Column Thickness t (mm)	Test Results K_1 (kN·m·rad ⁻¹)	Detailed Solid-Element Model Results K_2 (kN·m·rad ⁻¹)	Component-Based Model Results K_3 (kN·m·rad ⁻¹)	K_2/K_1	K_3/K_1
1	8	15,467	13,794	14,021	0.892	0.907
2	10	16,022	16,011	16,132	0.999	1.007
3	12	19,893	18,068	18,763	0.908	0.943

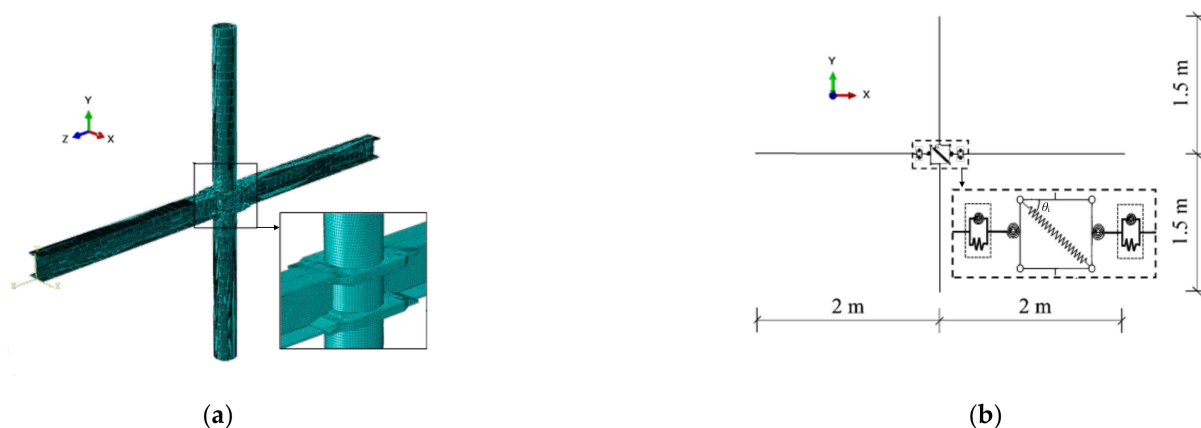


Figure 18. Different models of the CSS joint with circular tube columns to simulate the test specimen in reference [38]: (a) Detailed solid-element model; (b) Component-based model.

In Table 4, the initial rotational stiffness results of the test specimens, detailed solid-element models, and the component-based models are consistent with each other, which proves the applicability of the joint springs in the component-based model to simulate the H-shaped beam to circular-tube-column joints with CSS.

Based on the validation above, parameterized analysis of the initial rotational stiffness obtained from the component-based model was further conducted by varying the parameters in Equations (1)–(7). Compared with the numerical simulation results of the detailed solid-element models, the parameterized results are listed in Table 5. The results indicate that the initial rotational stiffness results of detailed solid-element models are consistent with those of the component-based models, which further verifies the applicability of the component-based model for the H-shaped beam to circular-tube-column joint with CSS.

Table 5. Parameterized analysis results of the initial rotational stiffness.

Specimen	h_b (mm)	B (mm)	t (mm)	h_r (mm)	l_1 (mm)	l_2 (mm)	Detailed	Component-	K_3/K_2
							Solid-Element	Based	
							Model	Model	
							K_2 (kN·m·rad ⁻¹)	K_3 (kN·m·rad ⁻¹)	
1	185						13,800	13,016	0.943
2	210	203	8	35	1407.5	1592.5	15,034	13,893	0.924
3	235						16,150	15,932	0.987
1		153					8926	9123	1.022
4	185	178	10	35	1407.5	1592.5	13,003	13,976	1.075
5		203					16,035	16,923	1.055
1			8				13,794	14,021	1.016
6	185	203	10	35	1407.5	1592.5	16,011	16,132	1.008
7			12				18,068	18,763	1.038
1				35			13,800	13,016	0.943
8	185	203	8	40	1407.5	1592.5	14,069	13,475	0.958
9				45			14,296	13,972	0.977
1						1592.5	13,800	13,016	0.943
10	185	203	8	35	1407.5	1842.5	11,917	10,334	0.867
11						2092.5	10,048	9452	0.941

4.2.2. The Stiffness of the Joint Springs after Yielding

(1) Bearing capacity

a. Rotational spring

According to reference [38], the calculation equation of the resultant tensile bearing capacity of the CSS and the column front shell (F_p^c) is given as:

$$F_p^c = f_{y,css} A_{s,min} + \frac{f_{y,c} t^2 l_w}{X_p} + 2(X_p + h_s) \frac{f_{y,c} t}{\sqrt{(1 + 2 \cos^2 \theta_c)}} \quad (8)$$

$$X_p = \sqrt{\frac{l_w t \sqrt{(1 + 2 \cos^2 \theta_c)}}{2}} \quad (9)$$

where $f_{y,css}$ is the yield strength of the CSS; $A_{s,min}$ is the minimum cross-sectional area of the CSS perpendicular to the force direction; $f_{y,c}$ is the yield strength of the column; l_w is the weld length; θ_c is half of the central angle corresponding to the arc length of the weld; and h_s is the height of the CSS.

The calculation equation for the bending bearing capacity $M_{p,s}^c$ of the joint rotational spring is given as

$$M_{p,s}^c = (f_{y,css} A_{s,min} + \frac{f_{y,c} t^2 l_w}{X_p} + 2(X_p + h_s) \frac{f_{y,c} t}{\sqrt{(1 + 2 \cos^2 \theta_c)}}) h_b \quad (10)$$

Combined with Equation (4), the rotation angle $\theta_{p,s}^c$ corresponding to the bending bearing capacity $M_{p,s}^c$ can be calculated as:

$$\theta_{p,s}^c = \frac{M_{p,s}^c}{k_s^c} = \frac{f_{y,css} A_{s,min} + \frac{f_{y,c} t^2 l_w}{X_p} + 2(X_p + h_s) \frac{f_{y,c} t}{\sqrt{(1 + 2 \cos^2 \theta_c)}}}{\frac{h_b E_s A_s}{2l_s} + \frac{h_b D}{4X_c L L_1}} \quad (11)$$

b. Panel zone spring

According to the Eurocode 3 [52] about the shear capacity of panel zones ($V_{p,pz}$), the tensile bearing capacity of the spring simulating the deformation of the panel zone ($F_{p,pz}^s$) can be deduced as

$$F_{p,pz}^s = \frac{V_{p,pz}}{\cos \theta_i} = \frac{f_{v,pz} A_v}{\cos \theta_i} \quad (12)$$

where $f_{v,pz}$ is the shear strength of the panel zone; and A_v is the shear area of the panel zone. For the circular tube column, the shear area of the panel zone (A_v) can be deduced as

$$A_v = 2A_c / \pi \quad (13)$$

where A_c is the cross-sectional area of the steel tube column when the thickness of the column is uniform.

Combined with Equation (7), the deformation $\Delta_{p,pz}^s$ corresponding to the tensile bearing capacity $F_{p,pz}^s$ can be calculated as:

$$\Delta_{p,pz}^s = \frac{F_{p,pz}^s}{k_{pz}^s} = \frac{2f_{v,pz} A_c \cos \theta_i}{\pi} \times \left(\frac{h_b^2 (l_1^3 + (l_2 - h_b)^3)}{3E_c I_c (l_1 + l_2)(l_1 + l_2 - h_b)} + \frac{k_c h_b (l_1 + l_2 - h_b)}{G_c A_c (l_1 + l_2)} \right) \quad (14)$$

(2) Post-yield stiffness

Based on the test results of the specimens in reference [38], the post-yield stiffness is only 0.090 to 0.103 of the initial stiffness of the CSS joint. Therefore, the post-yield stiffness of the joint springs in the component-based model can be safely defined as zero, which

means the simulation of the component-based model for CSS frames in progressive collapse is conservative.

4.3. Component-Based Model Response under a Sudden Column Removal Scenario

To validate the applicability of the component-based model for the frames with CSS joints in the dynamic nonlinear analysis under a column removal scenario, the detailed solid-element model of the CSS joint frame in Section 3 was remodeled by the component-based model method (shown in Figure 19). Under various loads in Table 1, the vertical displacements of the bottoms of the interior columns in the component-based model and the detailed solid-element model were compared. The comparison results are shown in Figure 20.

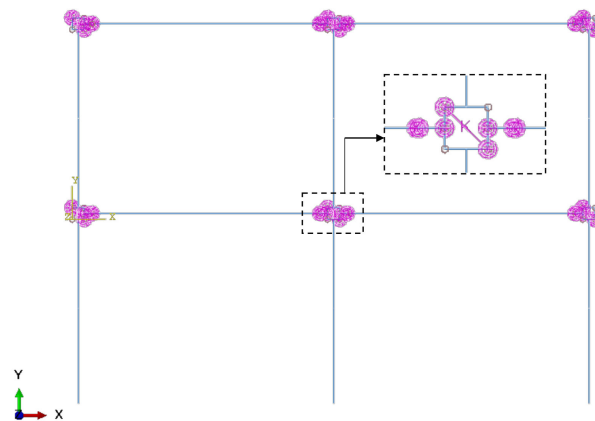


Figure 19. The component-based model (model M) remodeled from the detailed solid-element model B_c in Section 3.

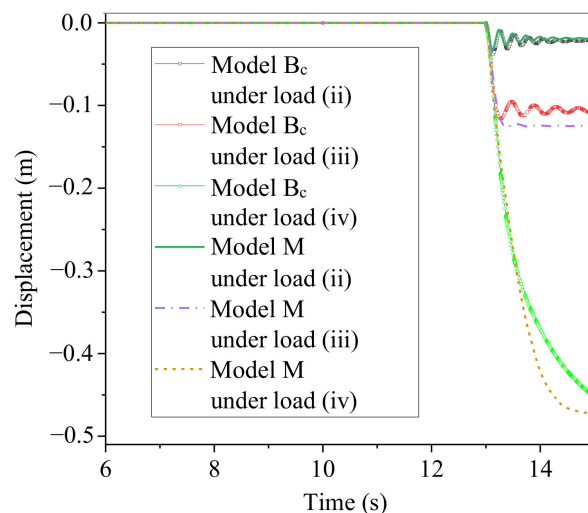


Figure 20. The vertical displacements of the bottoms of the interior columns in the component-based model (model M) and the detailed solid-element model (model B_c).

Figure 20 shows that in the dynamic nonlinear numerical analysis, the results of the component-based model are consistent with those of the detailed solid-element model, which proves the applicability of the component-based model in the dynamic nonlinear column removal analysis.

5. Dynamic Response Increase Factor

To further simplify the analysis process of CSS joint frames for progressive collapse prevention, the dynamic response of the structure can be equivalently analyzed by a static analysis method based on the recommendations in the DoD2010 guidelines [1]. Specifically, when the structure is designed to resist progressive collapse, the alternative load path method combined with a load combination of $1.2 DL + 0.5 LL$ can be used for dynamic analysis, while Ω_{DIF} ($1.2 DL + 0.5 LL$) can be used for static analysis. Ω_{DIF} is the dynamic increase factor (DIF) used in the nonlinear static analysis to consider the dynamic effect, DL is dead load, and LL is live load. The Ω_{DIF} of steel structures can be defined by the formula $\Omega_{DIF} = 1.08 + 0.76/(\theta_{pra}/\theta_y + 0.83)$, where θ_{pra}/θ_y is the ratio of the allowable plastic rotation θ_{pra} to the yield rotation θ_y . Generally, Ω_{DIF} can be conservatively selected as 2.0.

The formula proposed by the DoD 2010 [1] provides a usable method for calculating Ω_{DIF} , but the effect of the joint type is not taken into account in the formula. In order to obtain the Ω_{DIF} applicable to the CSS joint frames, the component-based model established in this paper can be used for efficient computation.

Under different levels of load, a series of nonlinear static and dynamic analyses were carried out using the component-based model. The ratio of the ultimate load of the static analysis to the ultimate load of the dynamic analysis is the dynamic response increase factor. For the convenience of description, different magnitudes of load can be represented by β ($1.2 DL + 0.5 LL$), where DL and LL are the dead load and the live load of the structure, respectively, and different load levels are obtained by varying β from 0.9 to the value corresponding to the case when the interior column displacement begins to increase.

Taking $DL = 3.2 \text{ kN}\cdot\text{m}^{-2}$ and $LL = 2 \text{ kN}\cdot\text{m}^{-2}$ as examples, the vertical displacements of the interior column in static and dynamic analyses under the gradually increasing load are shown in Figure 21. The relationships between the maximum vertical displacement and β in the dynamic and static analyses of the circular-tube-column frame are shown in Figure 22. Note that the β ($1.2 DL + 0.5 LL$) is a representation of the total load. If other loading cases with different live and dead loads are chosen, the same outcomes of the ultimate resistance load of static analysis and dynamic analysis of this frame can be obtained with the increase of β , and then the same dynamic increase factor of this component-based model can be obtained.

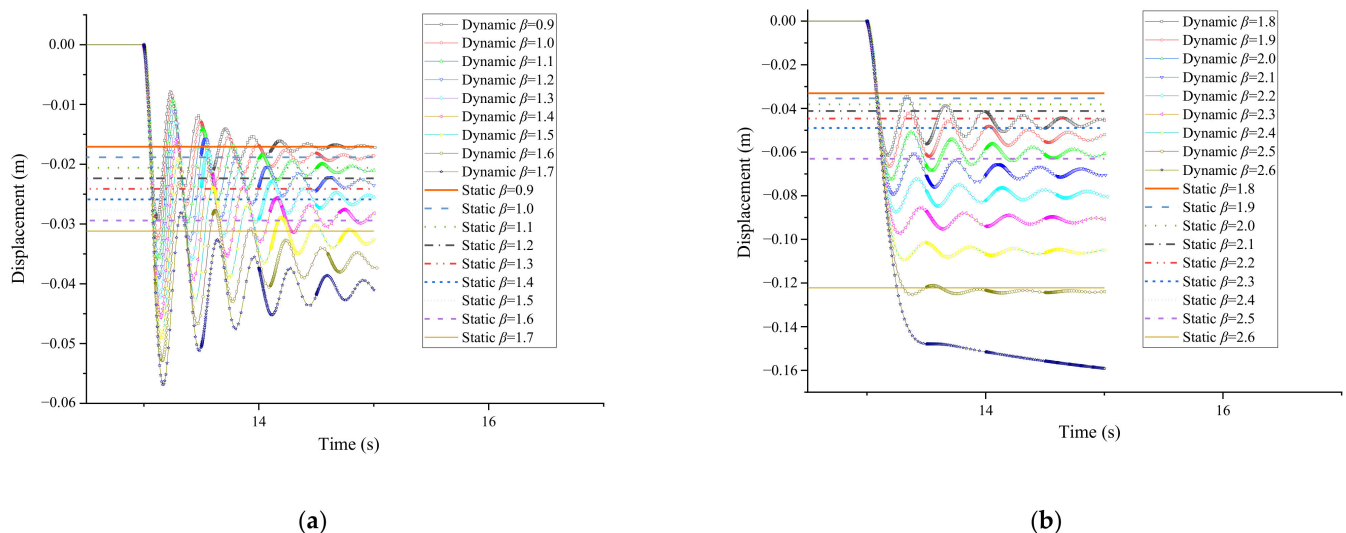


Figure 21. Displacements of the bottom of the interior column in dynamic and static analyses under gradually increasing loads ($\beta = 0.9$ – 2.6): (a) when $\beta = 0.9$ – 1.7 ; (b) when $\beta = 1.8$ – 2.6 .

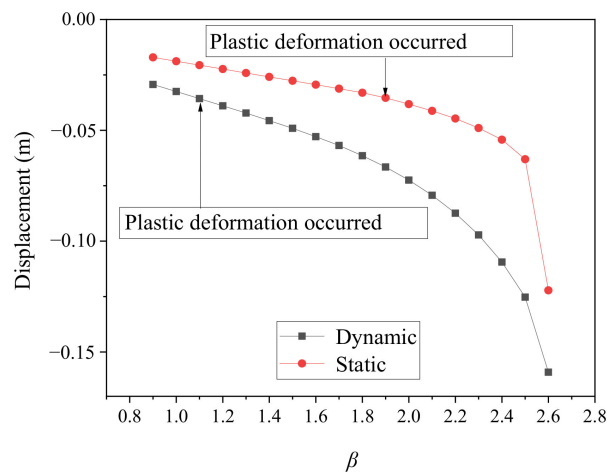


Figure 22. Maximum vertical displacement versus β in the dynamic and static analyses.

The calculation results show that for the circular-tube-column frame with CSS joints, when $\beta \leq 1$, the frame is elastic. In dynamic analysis, when $\beta = 1.1$, plastic deformation occurs; when $\beta = 2.6$, the vertical displacement of the bottom of the interior column increases rapidly at first, then slowly, and the displacement reaches 159 mm at 15 s. In the static analysis, when $\beta = 1.9$, plastic deformation occurs; when $\beta = 2.6$, the displacement of the interior column is merely 122 mm. Before the plastic deformation of the frame occurred, the ultimate load of static analysis is 1.9 (1.2 DL + 0.5 LL) and the ultimate load of dynamic analysis is 1.1 (1.2 DL + 0.5 LL). Therefore, the dynamic response increase factor (Ω_{DIF}) of 1.7, which is the ratio of 1.9 (1.2 DL + 0.5 LL) to 1.1 (1.2 DL + 0.5 LL), is suitable for a CSS joint frame with circular tube columns. This Ω_{DIF} is smaller than the 2.0 recommended in DoD 2010 [1] because the CSS joints reduce the maximum deformation of the frame during the progressive collapse.

6. Conclusions

In this paper, the force transfer mechanism of cast steel stiffener (CSS) frames under a column removal scenario was revealed by detailed solid-element models. Based on the mechanism analysis and the simplification principle that conforms to the frame characteristics, a practical component-based model suitable for the progressive collapse analysis of CSS frames was established and validated, and then the dynamic response increase factor for circular-tube-column frames with CSS joints was investigated by using this component-based model. The main conclusions are as follows:

- (1) The performance of the CSS joint frame for progressive collapse prevention is better than that of the fully welded joint frame. The CSS can delay the occurrence of plastic deformation of the CSS structures; the maximum and final values of the vertical displacement of the interior column in the CSS joint frame can be reduced, whether the frame is elastic, plastic, or collapsed after the sudden failure of the interior column.
- (2) In the case of sudden column removal, the stress distribution and the deformation mode of the CSS frame are revealed. Due to the relatively high rigidity and strength, the CSS can effectively bear the tensile loads from the flanges at beam ends and reduce the tensile loads borne by the front shell of the column, so the large strain of the column front shell is avoided. At the same time, due to the large strength and thickness of the cast steel stiffeners, the strain of the cast steel stiffeners is small. Therefore, the overall strain of the CSS joint is small and the stress distribution is relatively uniform. Moreover, plastic hinges at beam ends appear at locations farther away from columns in CSS joint frames, so the joints and the beam ends present relatively smooth-shaped curves after the sudden failure of the interior column.

- (3) Based on the stress distribution and the deformation mode of the circular-tube-column frames with CSS joints, a component-based model is proposed for the progressive collapse analysis. This efficient component-based model can simulate both the catenary effect and the construction details of the CSS joints for an overall steel frame under a column removal scenario. The equations of all the parameters of the springs in the component-based model are deduced based on the mechanical properties of the CSS joint frame, and the availability of the component-based model to simulate the dynamic nonlinear response of the CSS joint frame under a sudden column removal scenario is validated.
- (4) In order to further simplify the analysis process, dynamic effects can be incorporated into static analysis by using a dynamic increase factor for CSS joint frames. After plenty of static and dynamic analyses are conducted by using the component-based model, a dynamic increase factor of 1.7 suitable for the circular-tube-column frame with CSS is proposed. This dynamic increase factor is smaller than the 2.0 suggested in the DOD guidelines because the CSS joints reduce the maximum deformation of the frame during the progressive collapse.

To sum up, the advantages of CSS joints in resisting progressive collapse were fully demonstrated through force transfer mechanism analysis in this paper, and a simplified component-based model and a suitable dynamic response amplification factor were proposed to guide the design for progressive collapse prevention.

Author Contributions: Conceptualization, X.L. and M.L.; methodology, X.L. and M.L.; software, X.L. and M.L.; validation, X.L. and M.L.; formal analysis, X.L.; investigation, X.L.; resources, X.L. and M.L.; data curation, X.L. and M.L.; writing—original draft, X.L. and L.T.; writing—review and editing, X.L. and L.T.; visualization, X.L.; supervision, X.L.; project administration, X.L.; funding acquisition, X.L. All authors have read and agreed to the published version of the manuscript.

Funding: This research was funded by the Beijing Natural Science Foundation (Grant No. 8214048), the China Postdoctoral Science Foundation (Grant No. 2020M680320), and the Fundamental Research Funds for Beijing University of Civil Engineering and Architecture (Grant No. X21064).

Conflicts of Interest: The authors declare no conflict of interest.

References

1. DoD. *Unified Facilities Criteria (UFC): Design of Buildings to Resist Progressive Collapse, Unified Facilities Criteria (UFC) 4-023-03*; Department of Defense: Washington, DC, USA, 2010.
2. Pearson, C.; Delatte, N. Ronan point apartment tower collapse and its effect on building codes. *J. Perform. Constr. Fac.* **2005**, *19*, 172–177. [[CrossRef](#)]
3. Pantidis, P.; Gerasimidis, S. Progressive collapse of 3D steel composite buildings under interior gravity column loss. *J. Constr. Steel Res.* **2018**, *150*, 60–75. [[CrossRef](#)]
4. Zhou, H.; Li, J.; Spencer, B.F., Jr. Multiscale random fields-based damage modeling and analysis of concrete structures. *J. Eng. Mech.* **2019**, *145*, 04019045. [[CrossRef](#)]
5. Shabani, M.J.; Moghadam, A.S.; Aziminejad, A.; Razzaghi, M.S. Energy-based criteria for assessment of box-section steel columns against progressive collapse. *Structures* **2021**, *34*, 2580–2591. [[CrossRef](#)]
6. Khandelwal, K.; El-Tawil, S. Pushdown resistance as a measure of robustness in progressive collapse analysis. *Eng. Struct.* **2011**, *33*, 2653–2661. [[CrossRef](#)]
7. Gerasimidis, S.; Sideri, T. A new partial distributed damage method for progressive collapse analysis of buildings. *J. Constr. Steel Res.* **2016**, *119*, 233–245. [[CrossRef](#)]
8. Sideri, J.; Mullen, C.L.; Gerasimidis, S.; Deodatis, G. Distributed Column damage effect on progressive collapse vulnerability in steel buildings exposed to an external blast event. *J. Perform. Constr. Fac.* **2017**, *31*, 04017077. [[CrossRef](#)]
9. Wang, J.; Wang, W. Theoretical evaluation method for the progressive collapse resistance of steel frame buildings. *J. Constr. Steel Res.* **2021**, *179*, 106576. [[CrossRef](#)]
10. Alashker, Y.; Li, H.; El-Tawil, S. Approximations in progressive collapse modeling. *J. Struct. Eng.* **2011**, *137*, 914–924. [[CrossRef](#)]
11. Elsanadedy, H.M.; Abadel, A.A. High-fidelity FE models for assessing progressive collapse robustness of RC ordinary moment frame (OMF) buildings. *Eng. Fail. Anal.* **2022**, *136*, 106228. [[CrossRef](#)]
12. Li, L.; Wang, W.; Chen, Y.; Lu, Y. Experimental investigation of beam-to-tubular column moment connections under column removal scenario. *J. Constr. Steel Res.* **2013**, *88*, 244–255. [[CrossRef](#)]

13. Elsanadedy, H.; Alrubaidi, M.; Abbas, H.; Almusallam, T.; Al-Salloum, Y. Progressive collapse risk of 2D and 3D steel-frame assemblies having shear connections. *J. Constr. Steel Res.* **2021**, *179*, 106533. [[CrossRef](#)]
14. Mageirou, G.E.; Lemonis, M.E. Influence of imperfections on the progressive collapse of steel moment resisting frames. *J. Constr. Steel Res.* **2021**, *183*, 106744. [[CrossRef](#)]
15. Subki, N.E.A.; Mansor, H.; Hamid, Y.S.; Parke, G.A.R. The development of a moment-rotation model for progressive collapse analysis under the influence of tensile catenary action. *J. Constr. Steel Res.* **2021**, *187*, 106960. [[CrossRef](#)]
16. Daneshvar, H.; Driver, R.G. Performance evaluation of WT connections in progressive collapse. *Eng. Struct.* **2018**, *167*, 376–392. [[CrossRef](#)]
17. Zhong, W.; Meng, B.; Hao, J. Performance of different stiffness connections against progressive collapse. *J. Constr. Steel Res.* **2017**, *135*, 162–175. [[CrossRef](#)]
18. Qian, K.; Lan, X.; Li, Z.; Li, Y.; Fu, F. Progressive collapse resistance of two-storey seismic configured steel sub-frames using welded connections. *J. Constr. Steel Res.* **2020**, *170*, 106117. [[CrossRef](#)]
19. Li, H.; Cai, X.; Zhang, L.; Zhang, B.; Wang, W. Progressive collapse of steel moment-resisting frame subjected to loss of interior column: Experimental tests. *Eng. Struct.* **2017**, *150*, 203–220. [[CrossRef](#)]
20. Alrubaidi, M.; Elsanadedy, H.; Abbas, H.; Almusallam, T. Investigation of different steel intermediate moment frame connections under column-loss scenario. *Thin Walled Struct.* **2020**, *154*, 106875. [[CrossRef](#)]
21. Cortés, G.; Liu, J. Behavior of conventional and enhanced gravity connections subjected to column loss. *J. Constr. Steel Res.* **2017**, *133*, 475–484. [[CrossRef](#)]
22. Meng, B.; Zhong, W.; Hao, J.; Tan, Z. Improved steel frame performance against progressive collapse with infill panels. *J. Constr. Steel Res.* **2019**, *158*, 201–212. [[CrossRef](#)]
23. Chen, C.; Qiao, H.; Wang, J.; Chen, Y. Progressive collapse behavior of joints in steel moment frames involving reduced beam section. *Eng. Struct.* **2020**, *225*, 111297. [[CrossRef](#)]
24. Yu, Y.; Lan, L.; Chen, Z.; Huang, J. Mechanical and seismic behaviors of bottom-flange-bolted upper-flange-welded through-diaphragm connections. *J. Constr. Steel Res.* **2019**, *156*, 86–95. [[CrossRef](#)]
25. Han, Q.; Li, X.; Liu, M.; Spencer, B.F., Jr. Performance analysis and macromodel simulation of steel frame structures with beam-column joints using cast steel stiffeners for progressive collapse prevention. *Thin Walled Struct.* **2019**, *140*, 404–415. [[CrossRef](#)]
26. Feng, D.C.; Shi, H.R.; Parisi, F.; Brunesi, E.; Wang, C. Efficient numerical model for progressive collapse analysis of prestressed concrete frame structures. *Eng. Fail. Anal.* **2021**, *129*, 105683. [[CrossRef](#)]
27. Wang, F.; Yang, J.; Pan, Z. Progressive collapse behaviour of steel framed substructures with various beam-column connections. *Eng. Fail. Anal.* **2020**, *109*, 104399. [[CrossRef](#)]
28. Lin, S.C.; Yang, B.; Kang, S.B.; Xu, S.Q. A new method for progressive collapse analysis of steel frames. *J. Constr. Steel Res.* **2019**, *153*, 71–84. [[CrossRef](#)]
29. Ding, Y.; Song, X.; Zhu, H.T. Probabilistic progressive collapse analysis of steel frame structures against blast loads. *Eng. Struct.* **2017**, *147*, 679–691. [[CrossRef](#)]
30. Liu, M. Progressive collapse design of seismic steel frames using structural optimization. *J. Constr. Steel Res.* **2011**, *67*, 322–332. [[CrossRef](#)]
31. Dinu, F.; Marginean, I.; Dubina, D. Experimental testing and numerical modelling of steel moment-frame connections under column loss. *Eng. Struct.* **2017**, *151*, 861–878. [[CrossRef](#)]
32. Jiang, Z.Q.; Chen, M.L.; Yang, Z.S.; Li, X.Y.; Cai, C. Cyclic loading tests of self-centering prestressed prefabricated steel beam-column joint with weakened FCP. *Eng. Struct.* **2022**, *252*, 113578. [[CrossRef](#)]
33. Cheng, G.; Zhou, X.; Liu, J.; Chen, Y.F. Seismic behavior of circular tubed steel-reinforced concrete column to steel beam connections. *Thin Walled Struct.* **2019**, *138*, 485–495. [[CrossRef](#)]
34. Khanouki, M.M.A.; Sulong, N.H.R.; Shariati, M.; Tahir, M.M. Investigation of through beam connection to concrete filled circular steel tube (CFCST) column. *J. Constr. Steel Res.* **2016**, *121*, 144–162. [[CrossRef](#)]
35. Zhou, X.; Cheng, G.; Liu, J.; Yang, Y.; Chen, Y.F. Shear transfer behavior at the circular tubed column-steel beam interface. *Thin Walled Struct.* **2019**, *137*, 40–52. [[CrossRef](#)]
36. Mou, B.; Li, Y.; Wang, F.; Pan, W.; Zhao, Y. Flexural behavior of a novel high-strength RCFST column-to-column connection. *Thin Walled Struct.* **2021**, *159*, 107274. [[CrossRef](#)]
37. Yang, Z.; Deng, H.; Hu, X. Strength of longitudinal X-type plate-to-circular hollow section (CHS) connections reinforced by external ring stiffeners. *Thin Walled Struct.* **2018**, *131*, 500–518. [[CrossRef](#)]
38. Liu, M.; Li, X.; Han, Q.; Lu, Y. Theoretical research on force transmission mechanism and bearing capacity of round steel tube column-H-shaped steel beam cast-steel connection joint. *J. Build. Struct.* **2019**, *40*, 200–209. (In Chinese)
39. Khandelwal, K.; El Tawil, S.; Kunnath, S.K.; Lew, H.S. Macromodel-Based Simulation of Progressive Collapse: Steel Frame Structures. *J. Struct. Eng.* **2008**, *134*, 1070–1078. [[CrossRef](#)]
40. Lee, C.; Kim, S.; Lee, K. Parallel axial-flexural hinge model for nonlinear dynamic progressive collapse analysis of welded steel moment frames. *J. Struct. Eng.* **2010**, *136*, 165–173. [[CrossRef](#)]
41. Yu, J.; Tan, K.H. Experimental and numerical investigation on progressive collapse resistance of reinforced concrete beam column sub-assemblages. *Eng. Struct.* **2013**, *55*, 90–106. [[CrossRef](#)]
42. Bao, Y.; Kunnath, S.K.; El-Tawil, S.; Lew, H.S. Macromodel-based simulation of progressive collapse: RC frame structures. *J. Struct. Eng.* **2008**, *134*, 1079–1091. [[CrossRef](#)]

43. Fu, Q.; Yang, B.; Hu, Y.; Xiong, G.; Nie, S.; Zhang, W.; Dai, G. Dynamic analyses of bolted-angle steel joints against progressive collapse based on component-based model. *J. Constr. Steel Res.* **2016**, *117*, 161–174. [[CrossRef](#)]
44. Zhao, Z.; Jian, X.; Liang, B.; Liu, H. Progressive collapse assessment of friction damped post-tensioned steel frames based on a simplified model. *Structures* **2020**, *23*, 447–458. [[CrossRef](#)]
45. Liu, C.; Tan, K.H.; Fung, T.C. Component-based steel beam–column connections modelling for dynamic progressive collapse analysis. *J. Constr. Steel Res.* **2015**, *107*, 24–36. [[CrossRef](#)]
46. Stylianidis, P.M.; Nethercot, D.A. Modelling of connection behaviour for progressive collapse analysis. *J. Constr. Steel Res.* **2015**, *113*, 169–184. [[CrossRef](#)]
47. GB50017-2003; Code for Design of Steel Structures. Ministry of Housing and Urban–Rural Development of the People’s Republic of China: Beijing, China, 2003.
48. GB50009-2012; Load Code for the Design of Building Structures. Ministry of Housing and Urban–Rural Development of the People’s Republic of China: Beijing, China, 2012.
49. Khandelwal, K.; El-Tawil, S. Collapse behavior of steel special moment resisting frame connections. *J. Struct. Eng.* **2007**, *133*, 646–655. [[CrossRef](#)]
50. Han, Q.; Li, X.; Liu, M.; Spencer, B.F., Jr. Experimental investigation of beam-column joints with cast steel stiffeners for progressive collapse prevention. *J. Struct. Eng.* **2019**, *145*, 04019020. [[CrossRef](#)]
51. Wang, K.; Li, G.; Yang, T. The performance of restrained steel beams considering catenary effect under distributed loads (I)-Theoretical model. *Chin. Civ. Eng. J.* **2010**, *43*, 8–12. (In Chinese)
52. EN1993-1-1; Eurocode 3: Design of Steel Structures, Part 1–3: General Rules and Rules for Buildings. European Committee for Standardization: Brussels, Belgium, 2005.